ADVANCED HEALTHCARE MATERIALS
www.advhealthmat.de

Gelatin Nanoparticle-Injectable Platelet-Rich Fibrin Double Network Hydrogels with Local Adaptability and Bioactivity for Enhanced Osteogenesis

Zhixiang Mu, Kaiwen Chen, Shuai Yuan, Yihan Li, Yuanding Huang, Chao Wang, Yang Zhang, Wenzhao Liu, Wenping Luo, Panpan Liang, Xiaodong Li, Jinlin Song, Ping Ji, Fang Cheng, Huanan Wang, and Tao Chen**

Bone healing is a dynamic process regulated by biochemical signals such as chemokines and growth factors, and biophysical signals such as topographical and mechanical features of extracellular matrix or mechanical stimuli. Hereby, a mechanically tough and bioactive hydrogel based on autologous injectable platelet-rich fibrin (iPRF) modified with gelatin nanoparticles (GNPs) is developed. This composite hydrogel demonstrates a double network (DN) mechanism, wherein covalent network of fibrin serves to maintain material integrity, and self-assembled colloidal network of GNPs dissipates force upon loading. A rabbit sinus augmentation model is used to investigate the bioactivity and osteogenesis capacity of the DN hydrogels. The DN hydrogels adapt to the local environmental complexity of bone defects, i.e., accommodate the irregular shape of the defects and withstand the pressure formed in the maxillary sinus during animal's respiration process. The DN hydrogel is also demonstrated to absorb and prolong the release of the bioactive growth factors stemming from iPRF, which could have contributed to the early angiogenesis and osteogenesis observed inside the sinus. This adaptable and bioactive DN hydrogel can achieve enhanced bone regeneration in treating complex bone defects by maintaining long-term bone mass and withstanding the functional mechanical stimuli.

1. Introduction

Bone regeneration involves a cascade of biological events including early hemostasis and inflammation triggered by platelets and immune cells, matrix deposition, and mineralization induced by osteoblasts and bone remodeling driven by interplay between osteoblasts and osteoclasts.[1,2] This dynamic bone healing process has been elucidated to be actively regulated by the biochemical and biophysical signals. Biochemical signals include insoluble extracellular matrix (ECM) and soluble chemokines, cytokines, and morphogenetic growth factors.[2,3] Biophysical signals on the other hand are influenced by topographical and mechanical properties of ECM[4,5] and also the mechanical stimuli generating from physiological activities. In case of sinus, the physiological process of respiration and rhythmic movements can influence healing of bony defects.[1,6] The interplay of these

Z. Mu, S. Yuan, Y. Li, Prof. Y. Huang, Prof. C. Wang, Dr. W. Liu, Dr. W. Luo, Dr. P. Liang, Dr. X. Li, Prof. J. Song, Prof. P. Ji, Dr. T. Chen
Laboratory of Oral Diseases and Biomedical Sciences
Chongqing Municipal Key Laboratory of Oral Biomedical Engineering of Higher Education
Chongqing Medical University
Chongqing 401147, P. R. China
E-mail: chentao1985@hospital.cqmu.edu.cn

Dr. K. Chen, Prof. H. Wang
Key State Laboratory of Fine Chemicals
School of Bioengineering
Dalian University of Technology
No. 2 Linggong Road, High-tech District, Dalian 116024, P. R. China
E-mail: huananwang@dlut.edu.cn

Dr. Y. Zhang
Laboratory of Regenerative Biomaterials
Department of Biomedical Engineering
Health Science Center
Shenzhen University
Shenzhen, Guangdong Province 518037, P. R. China

Prof. F. Cheng
Key State Laboratory of Fine Chemicals
School of Chemical Engineering
Dalian University of Technology
No. 2 Linggong Road, High-tech District, Dalian 116024, P. R. China

The ORCID identification number(s) for the author(s) of this article can be found under https://doi.org/10.1002/adhm.201901469.

DOI: 10.1002/adhm.201901469

environmental cues along with biochemical factors play a pivotal role in determining bone formation and bone remodeling and presents as an enormous challenge toward bone regeneration. Enormous efforts have been made to replicate these intricate physiologically process for the purpose of bone tissue regeneration.[1,7]

On a biochemical level, the early presence of various growth factors (e.g., bone morphogenetic protein-2 (BMP-2), vascular endothelial growth factor (VEGF), and transforming growth factor-β (TGF-β)) within the formed blood clot at the defect sites is the dominant driving force to recruit stem cells and induce angiogenesis and osteogenesis.[3,8,9] In case of complex bone defects with critically sized defect area, irregular shape, and mechanical stimuli due to human's physiological activities presents as a limiting factor to achieve bone regeneration. To overcome this, bone grafts containing osteoinductive growth factors especially BMP-2 and BMP-7 have been extensively used for clinical treatment of bone defects.[8–11] However, severe side effects, high cost, and off-label use of inappropriate dose of these growth factors have restricted further applications in clinics.[11,12] Thus, to achieve sustained release of, preferably autologous, growth factors at a physiologically relevant dose is an important key to realize successful bone regeneration.

The so-called autologous blood-derived protein scaffolds, obtained by concentrating extract of platelets from patients' own blood, has recently emerged as a more effective and reliable therapy for the regeneration of skins, tendons, and bone tissues, which typically contain various instructive growth factors than application of exogeneous growth factors.[13,14] Among these autologous blood-derived protein scaffolds, injectable platelet-rich fibrin (iPRF) with concentrated growth factors can be used as an injectable formulation, which can gradually transform from a liquid phase to an elastic fibrin-based hydrogel.[15,16] The applications of iPRF or the other forms of autologous blood-derived protein scaffolds as scaffolds for the treatment of bone defects have shown limited success, most likely due to the substantially poor mechanical strength and rapid degradation of these scaffolds, which limit its single application to withstand complex mechanical environment and prolonged presentation of osteogenic signals for bone regrowth.[17] Attempts have been made to address these issues, by modifying the scaffolds with other biomaterials to improve the mechanical strength and delay biodegradation with sustained release of biochemical signaling molecules.[14,17] However, ideal bone scaffold is still lacking due to the problematic issues including i) difficulty to maintain long-term structural integrity when using injectable granular carriers,[18,19] ii) incapability to retain the long-term presence of growth factors,[19,20] and iii) mismatching mechanical properties of biomaterials to the local complex mechanical environment.[19,21]

From the biophysical aspect, scaffolds that mechanically mimics the natural ECM of bones and adapts to the irregular shape and local mechanical stimuli at the defect site is of tremendous significance for the regeneration of bone tissue.[4,5,22] A large number of previous studies have pointed out osteogenesis can be substantially affected by mechanical stimuli such as rhythmic compression or extension.[1,6] Particularly, stem cells have been demonstrated to be mechano-responsive, in which mechanical features such as stiffness, stress relaxation, and creep can significantly steer stem cell fate.[4,5,22,23] As shown previously, mesenchymal stem cells can induce osteogenic differentiation under 2D or 3D culture with hydrogels of proper stiffness.[5,22] More recent studies have further indicated the viscoelasticity of the ECM rather than the matrix's elasticity is the pivotal factor that determines the stem cell fate.[4,24] Cells can convert such mechanical signals from local environment into internal response via specific pathways. This further enables bone reconstruction and remodeling, which is known as "mechano-transduction."

Hydrogels have shown great potential to provide a physiologically relevant microenvironment for cell regrowth and tissue regeneration,[25] and also act as delivery vehicles for controlled drug release.[26] However, conventional permanently hydrogels with extensively high crosslinking density are typically more elastic rather than viscoelastic, and cannot adapt the local environmental complexity of bone defects,[24] i.e., to accommodate the irregular structure and topography of the defects, to replicate the mechanical signals of normal ECM, and to withstand the external forces resulting from regular physiological activities.[21] To overcome these limitations, hydrogels with local adaptability and long-term bulk stability have emerged as attractive biomaterials, which are typically formed by reversible interactions (e.g., electrostatic interactions, hydrophilic/hydrophobic interactions, hydrogen bonds, guest–host interactions).[21,27] As the term "adaptability" interpreted as the ability to withstand the complex mechanical environment and irregular shape, these adaptable hydrogels have shown desired viscoelasticity including shear-thinning and self-healing behavior resulting from the reversibility of physical linkage within the network.[28] However, these adaptable hydrogels have shown rather poor mechanical strength due to intrinsic feature of weak reversible bonds, thus restricting their widespread applications as biomaterials to spatially fill the bone defect rather than to substitute the defective load-bearing bones.[27,29] Therefore, it still remains a challenge to develop hydrogel biomaterials that are adaptable to the local structural and mechanical environment of bone defects.

Hereby, we proposed double network (DN) hydrogels by combining autologous iPRF with amphoteric gelatin nanoparticles (GNPs) that allow a "bottom-up" assembly of nanoparticles into an interconnected colloidal network. iPRF that is initially in liquid-like state was combined with the noncovalently crosslinked colloidal network that is shear-thinning and self-healing, which led to the formation of a composite hydrogel that possessed injectability and moldability within the initial 400 s as the polymerization of fibrin network was not completed yet.[30,31] The investigation of the structural and mechanical features of the composite hydrogels revealed a double network mechanism which rendered the hydrogels with toughness values and degree of deformation orders of magnitude greater than what they can achieve separately.[32] A rabbit sinus augmentation model was used to investigate the bioactivity and capacity of osteogenesis of the DN hydrogels, which showed desirable adaptability to the local environmental complexity of bone defects, i.e., to accommodate the irregular shape of the defects and to withstand the pressure formed in the maxillary sinus during animal's respiration. The DN hydrogel was also demonstrated to absorb and prolong the release of the bioactive

growth factors stemming from iPRF, which may contribute to the early angiogenesis and osteogenesis observed in the sinus cavity.

2. Results and Discussions

2.1. Mechanical Properties of GNPs-iPRF Composite Gels

To prepare GNPs-iPRF composite gels, iPRF was obtained from the whole blood of rabbits by centrifugation at 700 rpm for 3 min, which was initially a flowable liquid. We monitored the sol-gel transition process of iPRF by an oscillatory time sweep measurement using rheometer, and noticed a rapid increase of G' value (storage modulus) which crossed with G'' (loss modulus) after 10 min and eventually plateaued at $G' \approx 0.3$ kPa (**Figure 1**a and Figure S1, Supporting Information). This slow solidification process of iPRF allows it to be easily mixed with carrier materials such as GNPs simply by multiple cycles of extrusion using two connected syringes (**Scheme 1**).

GNPs have been demonstrated to form a rather elastic but also shear-thinning and self-healing colloidal gel due to the cohesive interactions between globally positively charged but locally amphoteric gelatin nanoparticles.[30,31] This allows colloidal gels of GNPs to be injectable/printable and moldable, as well as to be easily mixed with liquid-like materials by extrusion. Particularly, to obtain a mechanically strong colloidal gel, we prepared the gels with a GNP volume fraction φ above random close packing ($\varphi_{RCP} \approx 0.64$), corresponding to GNPs concentration of 12 w/v%. Such high φ can eliminate the structural change after shear-induced mixing and ensure the formation of the densely packed colloidal network by reversible interparticle bonds. As shown in Figure 1a, 12 w/v% GNPs formed quite weak colloidal gels with G' value of ≈1 kPa. Remarkably, the GNPs-iPRF composite gels resulted in much stronger gels with G' value of ≈10 kPa, one order of magnitude higher than that of pure GNPs colloidal gels or solidified iPRF. Moreover, the waiting time for the binary composite gel to completely solidify substantially reduced to ≈400 s as compared to iPRF, indicating the accelerated polymerization of fibrin network upon mixing with gelatin.[33] Before complete solidification, the GNPs-iPRF composite gels were shear-thinning and self-healing, enabling injectability and adaptability to irregularly shaped defect (Figure 1b and Figure S2, Supporting Information). Interestingly, the self-healing efficiency (defined as the recovered G' value relative to the initial G') for the composite gels without triggering fibrinogen's polymerization (by adding sodium citrate to block the hemostasis process) reached up to ≈90%, significantly higher than pure GNPs colloidal gels of the same concentration (≈73%) (Figure S3, Supporting Information); we speculated this can be related to the enhanced interparticle interactions between GNPs caused by the depletion force upon mixing GNPs with iPRF and/or cohesive interactions between gelatin and fibrin.[34] The self-healing efficiency (defined as the recovered G' value relative to the initial G') substantially declined to <30% (Figure 1c).

We further evaluated the self-healability of GNPs-iPRF gels upon cutting, the gels were cut into small pieces and put (unstained or stained by purple dye) into direct contact at their freshly cut interface. For the composite gels before complete solidification, the cracks self-healed within a few minutes at room temperature induced by the reversible interparticle bonds. In contrast, the composite gels gradually lost the self-healability after the complete solidification of iPRF (Figure 1d and Figure S4, Supporting Information), since the covalent bonds of fibrin network dominated, and interrupted the reversibility of interparticle bonds within the network. Apparently, the GNPs-iPRF composite gels were highly elastic and stiff, evidenced by the frequency-independent behavior measured by rheology, which was opposite to solidified iPRF showing more frequency-dependent behavior (Figure 1e). Especially, the inherent deformability of soft gelatin nanoparticles allowed the preparation of highly jammed colloidal dispersions in iPRF with volume fractions up to 1 as the deformable soft GNPs can fill into the interparticle voids. As shown in Figure 1f, GNPs concentrations above 12 w/v% ($\varphi \approx 0.6$) in iPRF can form highly stiff gels with G' value reaching up to 28 ± 4 kPa (20 w/v% of GNPs in the composite gels, corresponding to $\varphi \approx 1$).

We further characterized the mechanical properties of GNPs-iPRF composite gels (12 w/v% of GNPs) using conventional compression and tensile tests. The composite gels showed a linear-elastic response followed by a brittle fracture mode upon compressive loading, with the compressive modulus E and strength σ_c of 32.7 ± 4.6 and 34.1 ± 4.3 kPa, respectively, and the fracture strain of 50% (Figure S5, Supporting Information). In comparison, the colloidal gels showed a similar elastic behavior upon compression but less stiffness with E and σ_c of 9.2 ± 2.7 and 5.6 ± 0.8 kPa, respectively, whereas the iPRF showed an even weaker and easily deformed gel with E and σ_c of 0.9 ± 0.1 and 1.1 ± 0.1 kPa, respectively. We calculated the fracture energy upon compression and tensile by the integrated area under the loading curve, the composite gels presented significantly higher fracture energy of 9.2 ± 2.2 kJ m^{-3} as compared to GNPs colloidal gels (1.7 ± 0.2 kJ m^{-3}) and solidified iPRF (0.5 ± 0.1 kJ m^{-3}) (Figure 1g). Remarkably, the tensile tests also revealed a purely elastic response for the composite gels evidenced by the linear stress–strain curve and the absence of any plastic deformation (Figure 1h), with the tensile modulus E and strength σ_t of 25.3 ± 4.1 and 8.1 ± 1.3 kPa, respectively. In contrast, solidified iPRF gels showed weaker mechanical properties with E and σ_t of 1.5 ± 0.3 and 1.2 ± 0.2 kPa, respectively; meanwhile, the colloidal gels were more elastic than iPRF with E and σ_t of 14.1 ± 3.1 and 2.5 ± 0.2 kPa, respectively. The composite gels also exhibited enhanced stretchability with the fracture strain up to ≈40%, slightly lower than iPRF (fracture strain of 56.1 ± 7.1%), but considerably higher than pure GNPs colloidal gels of 9.7 ± 0.8%. Besides, the GNPs-iPRF composite gels showed higher fracture energy of 1.6 ± 0.4 kJ m^{-3} as relative to pure GNPs colloidal gels (0.09 ± 0.01 kJ m^{-3}) and iPRF (0.14 ± 0.03 kJ m^{-3}) (Figure 1i). The significantly enhanced mechanical properties of the composite gels reminded us of the design principle and mechanical behavior of DN hydrogels, which typically showed remarkably enhanced toughness values and degree of deformation than each component can achieve separately. Inspired by this, we speculated that the fibrin network in the GNPs-iPRF composite gels serves as a primary covalent network to maintain material integrity, while GNPs formed a secondary colloidal network to provide sacrificial

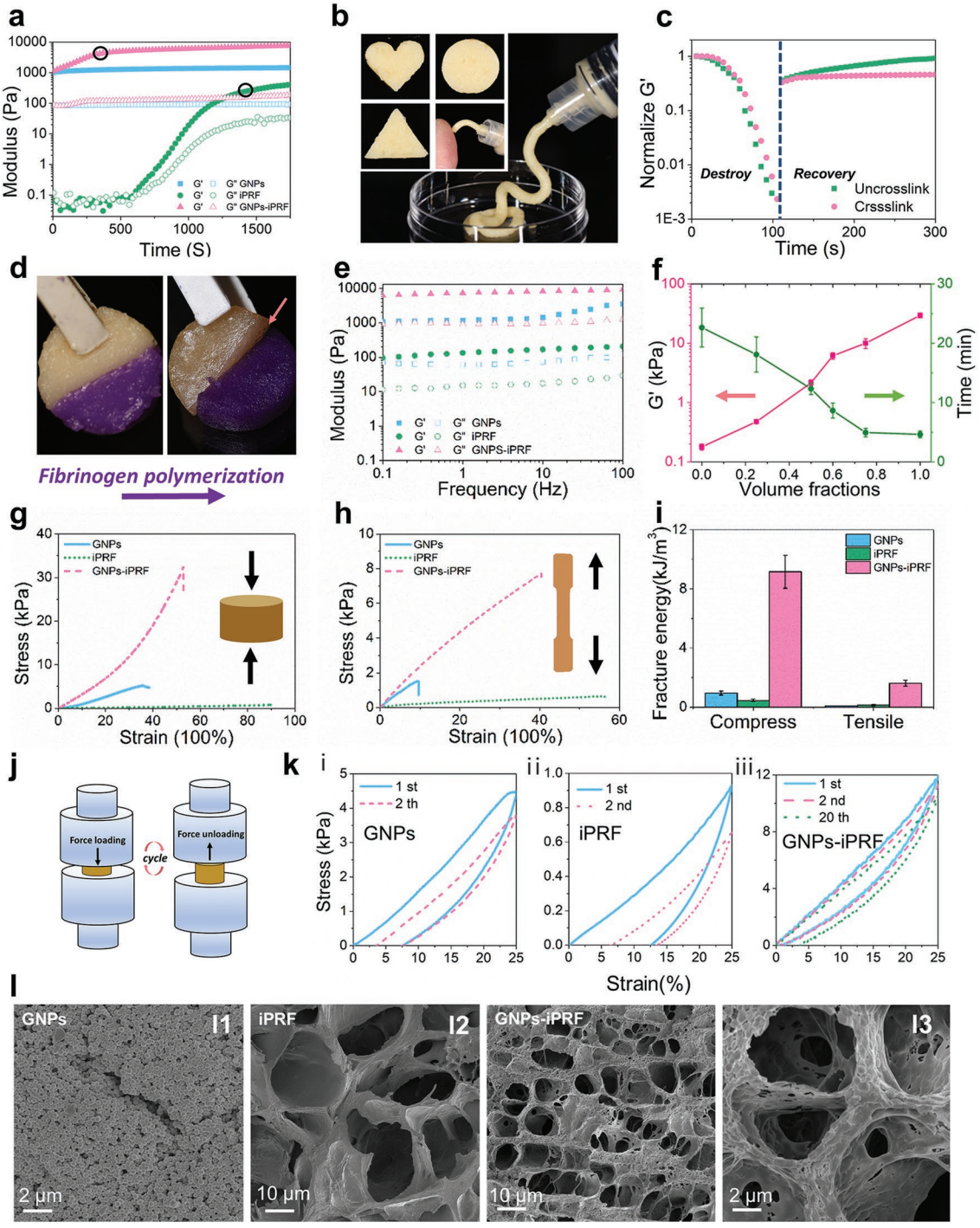

Figure 1. The structural and mechanical properties of GNPs-iPRF composite hydrogels. a) Triggered self-polymerization of iPRF and GNPs-iPRF gels (time sweep at 0.5% strain and 1 Hz frequency), as reflected by the sharp increase of G' and G'' value and the excess of G' relative to G'' indicating a sol-gel transition. b) Images showing the injectability and moldability of GNPs-iPRF gels when the fibrin network was not yet solidified. c) Evolution of storage modulus of GNPs-iPRF gels before (denoted as "uncrosslink") and after iPRF network formation (denoted as "crosslink") during the destructive shearing (oscillatory strain sweep with increasing strain from 0.1% to 1000% with a fixed frequency of 1 Hz) and recovery (oscillatory time sweep at 0.5% strain and a frequency of 1 Hz for 200 s). d) The corresponding images showing the self-healing behavior of the GNPs-iPRF gels before and after solidification. e) Frequency dependence of storage (solid symbol, G') and loss (open symbol, G'') modulus of GNPs, iPRF, and GNPs-iPRF gels. (GNPs concentration of 12 w/v%.) f) The storage modulus and time of solidification for GNPs-iPRF gel as a function of volume fractions of GNPs in the composites. g) The stress–strain curves of compressive, and h) tensile measurements at a strain rate of 0.021 1 s^{-1} for the GNPs, iPRF, and GNPs-iPRF gels. i) The fracture energy calculation based on compressive and tensile measurements of GNPs, iPRF, and GNPs-iPRF gels ($n = 3$). j,k) The hysteresis curves of different hydrogels upon cyclic compressive loading and unloading. l) The scanning electron microscopic photographs showing the representative microstructures of GNPs (l1), iPRF (l2), and GNPs-iPRF (l3) gels.

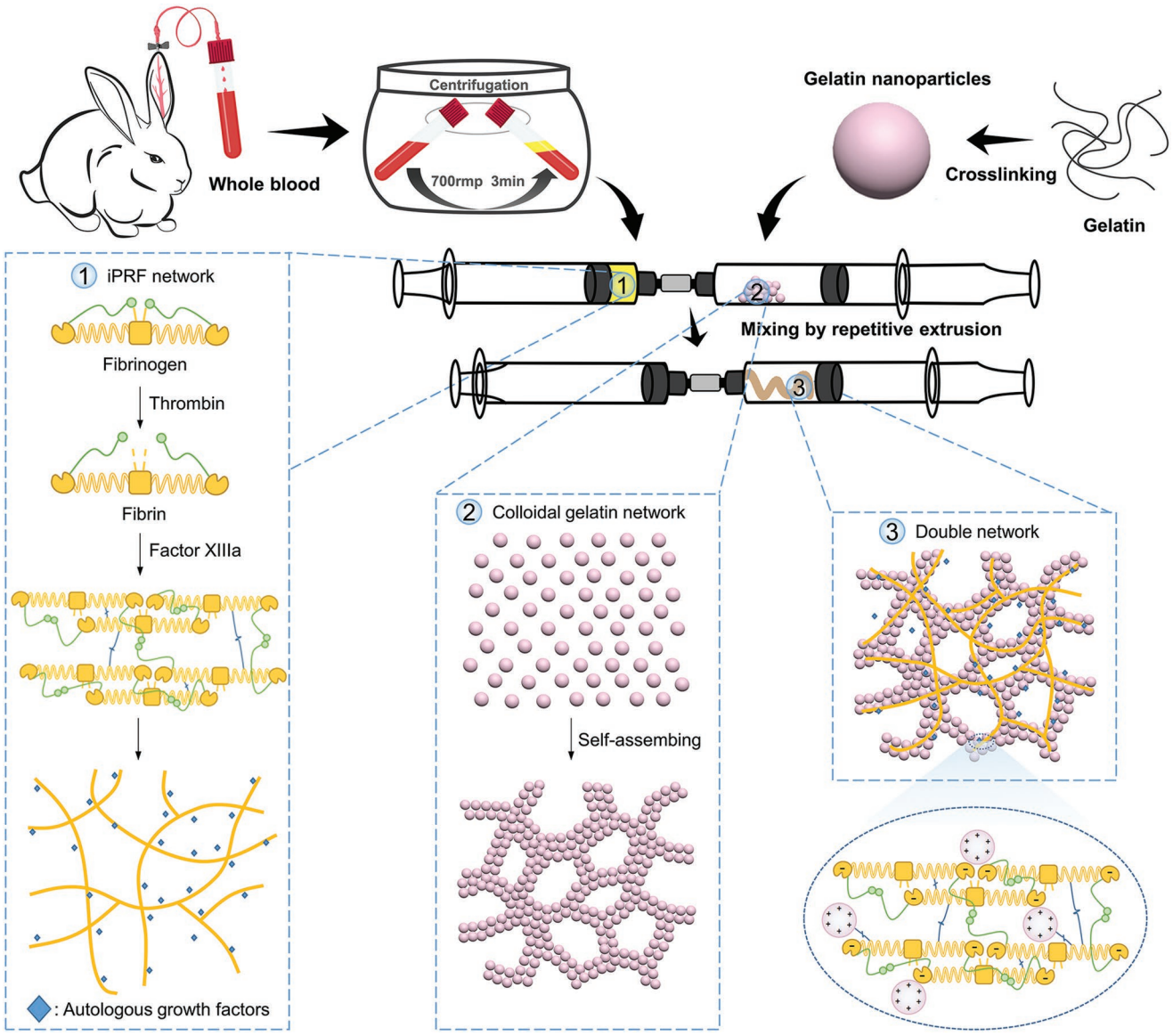

Scheme 1. Schematic diagram of the design and preparation of double network hydrogels composed of GNPs and injectable platelet-rich fibrin (iPRF). The whole blood was taken from rabbits and centrifuged at 700 rpm for 3 min, a yellowish liquid-like iPRF at the upper layer of the blood was obtained and immediately transferred into a syringe and mixed with the freeze-dried GNPs by repetitive extrusion of the mixtures in two connected syringes until the consistency was even. The mixture was injectable and moldable within 400 s, until the solidification of the composite hydrogel triggered by polymerization of fibrin network, realizing the formation of double network hydrogels composed of GNPs and iPRF. The cartoons display the mechanism of the formation of ① platelet-rich fibrin network, ② colloidal network of GNPs, and ③ the DN hydrogel composed of GNPs and iPRF. For the composite system of iPRF and GNPs, after mixing the two components, the polymerization reaction between fibrinogen and thrombin in iPRF led to the formation of fibrin network, which was adhesive to the positively charged GNPs due to electrostatic and hydrophobic interactions between the two components.

bonds to dissipate energy, thus cooperatively leading to the formation of much tougher hydrogels.

Therefore, we explored the capacity for energy dissipation of composite gels by performing cyclic compression tests. The GNPs-iPRF composite gels can stand the repetitive applications of the stress of ≈12 kPa and a strain of 25% (≈50% of the yield strain), and can rapidly recover to the original shape upon unloading (Figure 1j,k(iii) and Figure S6, Supporting Information). We observed complete and overlapping hysteresis loops during the multiple loading/unloading processes in the stress–strain curves for the composite gels. We quantified the efficiency of energy dissipation by calculating the ratio between the integrated area in the hysteresis loop and that under the loading curve, and found that the energy dissipative efficiency of GNPs-iPRF reached 20% and the mechanical recovery ≈95% after 20th cycle compression; this suggested that the composite gels were highly elastic and antifatigue. In comparison, the colloidal gels (12w/v% GNPs) and iPRF gels were rather viscoelastic, characterized by unrecovered plastic deformation of 7.5% and 15.1% (compression strain = 25%),

respectively (Figure S7, Supporting Information). We speculated the improved gel mechanics of the hybrid network to be attributed to the formation of an interpenetrated network by gelatin colloids and fibrin. To demonstrate our hypothesis, we further studied the microstructure of the GNPs-iPRF composite gels. The scanning electron microscope (SEM) images showed that solidified iPRF presented a highly porous network (Figure 1l2). The composite gels depicted a porous network formed by assembled gelatin nanoparticles and fibrin fibers interconnected with each other, indicating that there might be cohesive interactions between the two components (Figure 1l3).

2.2. Exploration of the Double Network Mechanism Based on GNPs-Fibrin System

We further used pure fibrin, which is the key component to trigger solidification of iPRF, to combine with GNPs to form the composite gels. This allowed to simplify the composition of the gels and to study the network mechanics based on a biphasic system. We labeled GNPs and fibrinogen with rhodamine and fluorescein, respectively. This allowed real-time monitoring the formation of gel network using confocal microscopy. To clearly visualize the network structure, rather dilute gel network was prepared by dispersing 1 w/v% GNPs (corresponding to volume fraction φ of ≈5%) in 5×10^{-3} M HEPES buffer containing 0.1 w/v% fibrinogen combined with 2 U mL^{-1} thrombin. As shown in **Figure 2**a, 0.1 w/v% fibrinogen led to a uniformly distributed porous fibrin network after reacting with 2 U mL^{-1} thrombin and quenching for 1 min, whereas 1 w/v% GNPs also formed an interconnected particulate network after dispersed in neutral pH due to the cohesive interparticle forces.[31] In comparison, we observed the formation of an interconnected network with higher porosity and thicker network strands after mixing GNPs with fibrinogen and thrombin. More importantly, the separate fluorescent channels for rhodamine and fluorescein both depicted an interconnected topology which overlapped with each other. This indicated the high affinity between two components which might be the driving force for the formation of double network (Figure 2a). We further evaluated the network topology by quantifying the average strand thickness r, average strand length ξ, and node density ν (Figure S8, Supporting Information).[35] The biphasic gels exhibited a thicker strand thickness and longer strand length ($r = 8.9 \pm 1.5$ μm, $\xi = 18.3 \pm 2.1$ μm) in comparison to pure fibrin ($r = 4.6 \pm 1.3$ μm, $\xi = 12.1 \pm 1.3$ μm) and colloidal gels ($r = 2.3 \pm 0.6$ μm, $\xi = 7.6 \pm 1.1$ μm). The node density of the biphasic gels (9.4 ± 2.3 N μm^{-2}) were lower than that of pure fibrin (21 ± 4.6 N μm^{-2}) but similar to colloidal gels (8 ± 3.9 N μm^{-2}). Combining these structural properties with the mechanical properties of the composite gels, we noticed that the higher strand length ξ and lower node density ν, surprisingly, resulted into the stronger biphasic network as compared to each single component. This should be attributed to the higher spring constant $\kappa(\xi)$ which was positively correlated with the G' on value for the double network gels,[36] in which two components collaboratively established much thicker and tougher strands in the network driven by the strong cohesive forces such as electrostatic and hydrophobic interactions.

Further SEM and laser scanning confocal microscopy images of the biphasic gels prepared at higher concentration (2 w/v% fibrinogen in combination with 20 U mL^{-1} thrombin, with 12 w/v% GNPs) showed the formation of a sponge-like porous structure with micrometer-sized fibrin fibers adhered to the densely packed GNPs (Figure 2b3 and Figure S9, Supporting Information). This confirmed the cohesive interactions between fibrin and GNPs (Figure S10, Supporting Information). Remarkably, at higher concentration, the packing density and the branch thickness of the double network gels were much higher than that of pure colloidal and fibrin network, which was beneficial to the mechanical properties of the gels.

Further investigation of the mechanical properties of the GNPs-Fibrin (GNPs-Fib) biphasic gels revealed similar behavior to that of GNPs-iPRF gels. Before adding thrombin to trigger the polymerization of fibrinogen, GNPs-Fib gels showed similar behavior to that of GNPs colloidal gels characterized by remarkable self-healing capability (≈90% self-healing efficiency). Once fibrin network solidified, the biphasic gels became highly elastic and stiff at the cost of losing self-healability (Figure S11, Supporting Information). The compression and tensile tests also confirmed the improved mechanical properties of the GNPs-Fib gels (Figure 2c,d). Typically, 2 w/v% fibrin gels (similar fibrin concentration to the blood) were rather weak with compressive elastic modulus E and strength σ_c of 0.5 ± 0.1 and 4.4 ± 0.5 kPa, while GNPs colloidal gels were stiffer ($E = 9.2 \pm 2.7$ kPa, $\sigma_c = 5.6 \pm 0.8$ kPa) but rather brittle as evidenced by the fracture strain of 35.7%. In comparison, the biphasic gels were significantly more elastic, as reflected by the higher compressive elastic modulus of 27.9 ± 1.9 kPa, fracture strain of 62.2 ± 11.3% (twice of GNPs colloidal gels) and the fracture stress of 31.6 ± 5.2 kPa (six times of GNPs, eight times of fibrin). The tensile tests revealed a purely elastic response of GNPs-Fib gels, reflected by the linear stress–strain curve. Moreover, the biphasic hydrogels were much tougher in comparison to fibrin gels and colloidal gels. The combination of continuous fibrin network with reversible colloidal one allowed high degree of energy adsorption upon loading but also the maintenance of structural integrity at large deformation. This can be evidenced by high fracture energy of the biphasic gels under compression or tension, even one order of magnitude higher than what each component can achieve separately (Figure 2e). In general, these structural and mechanical properties of the biphasic gels demonstrated that the combination of GNPs with iPRF led to the formation of a double network hydrogel, which possessed significantly improved network toughness to enable long-term bulk stability, desirable injectability to be applied in minimal invasive surgery, and adaptability to locally satisfy the needs for shape and mechanical strength. Conventional composite colloidal gels are typically composed of a continuous particulate network dispersed in a liquid, in which different colloids with interparticle attractions (e.g., electrostatic and hydrophobic/hydrophilic interactions) serve as building blocks to assemble into constructs with desirable mechanical strength and structural integrity.[30,37,38] However, these purely particulate networks invariably showed limited deformability and fatigue resistance due to the short effective range of these physical interactions. On the other hand,[39] traditional composite gels with colloidal particles dispersed in a continuous polymeric

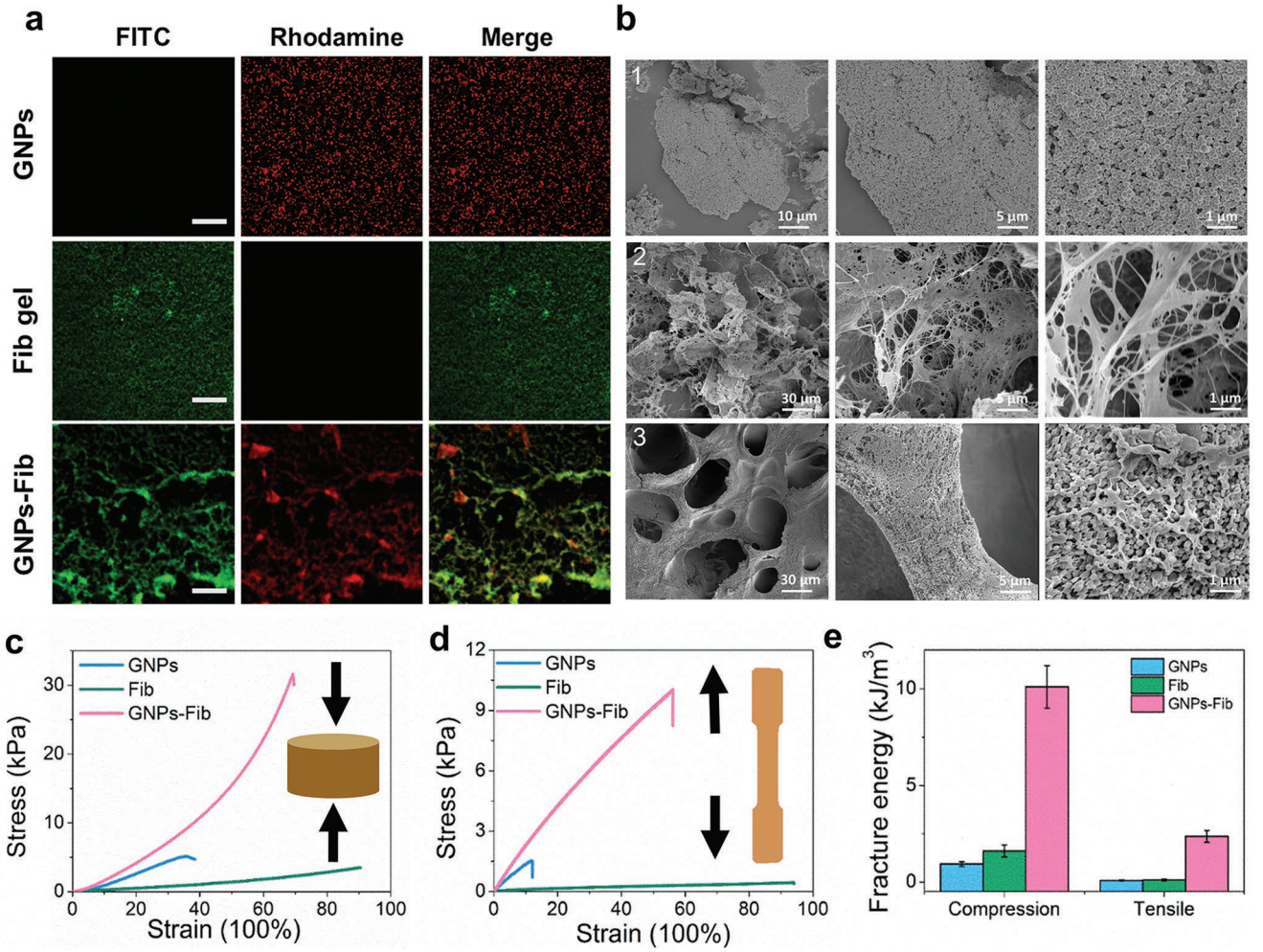

Figure 2. The structural and mechanical properties of GNPs-Fib biphasic hydrogels. a) Representative confocal microscopic images showing the microstructure of pure fibrin network, self-assembled GNPs colloidal network, and double network composed of GNPs-Fib (GNPs concentration of 1 wt%, fibrin of 0.1 wt% in combination of 2 U mL^{-1} thrombin, in 5×10^{-3} M HEPES buffer). The GNPs and fibrin were fluorescently labeled by rhodamine and FITC, respectively; this allowed real-time monitoring of the formation of gel network using confocal microscopy. 0.1 w/v% fibrinogen led to a uniformly distributed porous fibrin network after reacting with 2 U mL^{-1} thrombin and quenching for 1 min, whereas 1 w/v% GNPs also formed an interconnected particulate network after dispersed in neutral pH due to the cohesive interparticle forces. For mixture of GNPs and fibrin, an interconnected network with higher porosity and thicker network strands was observed. The separate fluorescent channels for rhodamine and FITC both depicted an interconnected topology which overlapped with each other; this indicated the high affinity between two components which might be the driving force for the formation of double network (Scale bar = 50 μm). b) Representative scanning microscopic images of the freeze-dried GNPs (1), fibrin (2), and GNPs-Fib DN gels (3) at different magnifications. The fibrin network showed a highly porous but connected architecture consisting of thin films and fibers, while the double network GNPs-Fib hydrogels showed a rather low porosity composed of densely packed GNPs connected with fibrin fibers. d,e) The representative stress–strain curves of compressive and tensile measurements on GNPs, fibrin, or GNPs-Fib hydrogels. Strain rate = 0.1 1 s^{-1}. f) The corresponding fracture energy calculated based on compression and tensile tests for different hydrogels ($n = 3$).

network normally showed reinforcement effect resulting from the introduction of solid colloids, which were sporadically dispersed in the polymer network. This strategy could enhance the mechanical strength of the resulting composite to a certain extent, but might also occasionally compromise the mechanical performance due to the disturbed homogeneity of continuous phase or phase separation between the two components. In comparison, our strategy of double network GNPs-iPRF composite gels showed substantially higher mechanical properties resulting from the formation of two interpenetrated networks of covalent fibrin network and reversible GNPs colloidal network. Specifically, the gelatin colloids formed a continuous particulate network existed simultaneously with the polymeric fibrin network, which provided the resulting composites improved injectability/moldability but also enhanced toughness by enabling energy dissipation upon loading.

2.3. GNPs-iPRF Gels for Bone Formation in Sinus Augmentation Models

The reconstruction of irregular-shaped bone defects is one of the most challenging cases in orthopedics, maxillofacial, and dental surgery. This requires bone substitutes to be

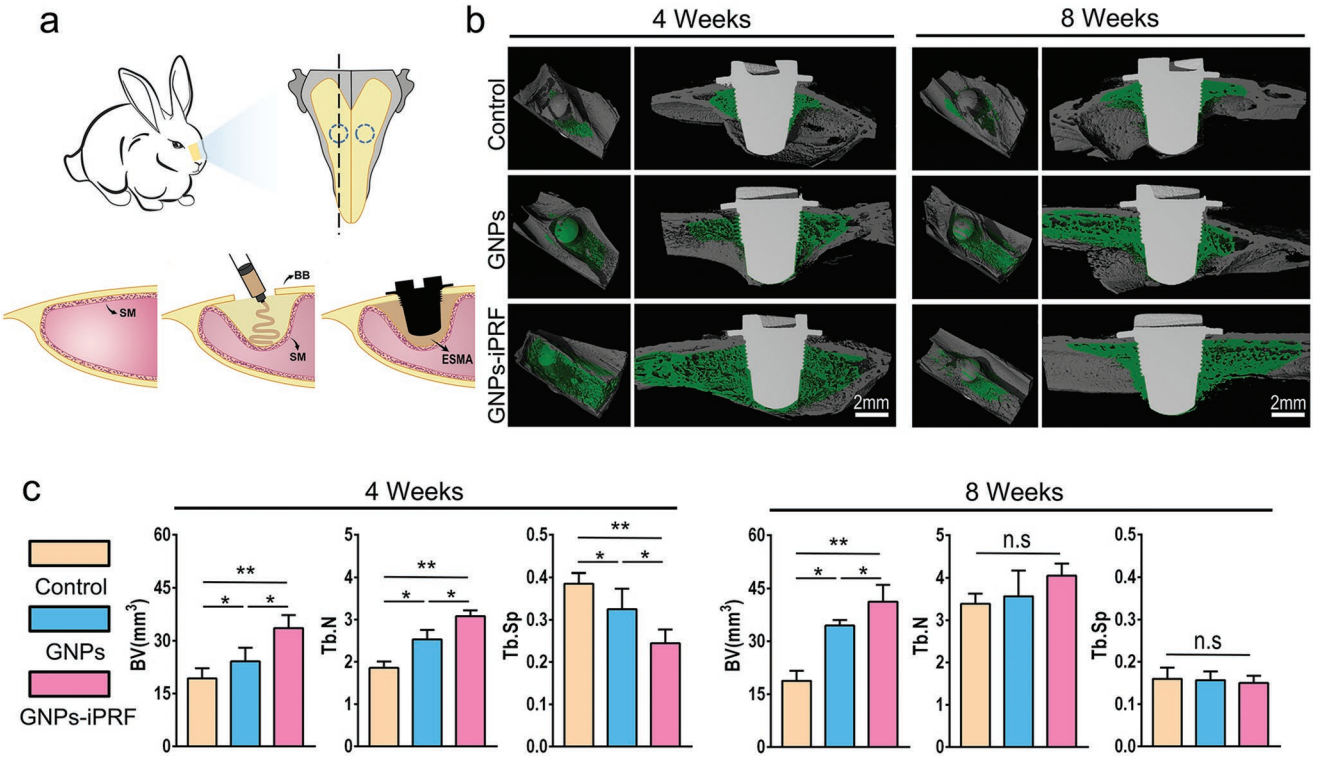

Figure 3. Evaluation of bone formation in a New Zealand rabbit sinus augmentation model treated with GNPs-iPRF DN hydrogels. a) Scheme showing the treatment of sinus augmentation. Briefly, a 5 mm cylinder-shaped bony defect was prepared bilaterally on the sagittal midline of the nasal bone. Schneiderian membrane was carefully lifted to separate it from the basal bone to form an irregular-shaped defects. The colloidal gels were then injected into the cavity using a syringe, followed by the placement of implants. b) Micro-CT examination at 4 and 8 weeks post-implantation showed that the GNPs-iPRF group exhibited significantly more new bone formation than the other two groups. Dark gray represents the basal bone, green represents the new bone formation, and light gray represents the implant. c) Bone volume (BV), trabecular number (Tb.N), trabecular separation (Tb.Sp) were measured ($n = 3$). The results revealed that more bone formation and more compact trabecular bone were detected at four weeks in GNPs-iPRF group. At eight weeks, more bone formation was observed in GNPs-iPRF while there was no statistical difference regarding Tb.N and Tb.Sp among three groups. SM: Schneiderian membrane, BB: basal bone, ESMA: elevated Schneiderian membrane area, * $P < 0.05$, ** $P < 0.01$.

preferably injectable and adaptable.[9,40] Sinus augmentation, typical treatment to generate bone tissues in sinus cavity for the later insertion of dental implants, is a typical maxillofacial surgery that calls for the tissue regeneration at irregular-shaped bone defects.[9] Traditional treatment for sinus augmentation is to elevate the Schneiderian membrane from basal bone and fill the sinus cavity with granular bones substitutes including autogenous or decellularized allogenous/exogenous bones, or synthetic bone grafts such as hydroxyapatite or tri-calcium phosphates, which has shown disadvantages including poor osteogenic efficacy, mismatched material degradation versus bone regrowth, difficulty in filling irregular-shaped cavity, and unfavorable clinical handling properties.[9,12]

Here in this study, we took advantages of the injectability, adaptability to local structural and mechanical conditions, and capacity of sustained release of biomolecules from the GNPs-iPRF hydrogels, and used these gels for the treatment of sinus augmentation in a rabbit model. In this regard, we compared the GNPs-iPRF gels, with pure GNPs colloidal gels or without any filler as control accordingly. However, the sinus cavity in control group was not interpreted as "empty" here. Due to the elevation of SM without filling of the grafts, which was taken as a normal surgical attempt, blood would replenish into the sinus defect and subsequently changed into blood clots. The sinus was subsequently implanted by a titanium implant at the basal bone sites (**Figure 3**a and Figure S15a, Supporting Information). At different time points, the maxillofacial bones from the sacrificed animals were explanted for micro-CT examination. As shown in Figure 3b, the cone-shaped de novo bones that protruded toward sinus cavity were observed to be surrounding the titanium implants for all three experimental groups. Remarkably, the sinus cavities treated with GNPs-iPRF hydrogels led to significantly higher amount of new bone formation in the elevated Schneiderian membrane area (Figure 3b) as compared to GNPs gels and the control. We then quantified the volume of newly formed bones (denoted as BV), the number of trabecular bones (denoted as Tb.N), and trabecular separation defined as the space between trabecular bones (denoted as Tb.Sp) by processing the micro-CT data. At four weeks, the GNPs-iPRF group exhibited significantly higher values for BV and Tb.N but lower value for Tb.Sp as compared to GNPs and control groups; this suggested the DN hydrogels could be equipped with highly bioactive and osteogenic properties (Figure 3c). Interestingly, even the implantation of pure GNPs colloidal gels resulted into the formation of significantly higher volume of new bone than the control. We speculated that, due to the capacity of GNPs to absorb protein-based growth factors by forming electrostatic interactions or hydrogen bonds between proteins and gelatin

macromolecules,[8,29,37,41] GNPs could absorb the bioactive molecules from the bloods and continuously release them at the defect sites, which can favor the bone regrowth. Whereafter, the effect of controlled-released factors from GNPs-iPRF was validated through ELISA kit.

To further histologically evaluate the newly formed bone tissues, we further performed Stevenel's blue and Van Gieson's picrofuchsin staining (VG staining) on hard tissue sections, in which osteoid was stained by blue dyes and red dyes were for the staining of matured bone tissues. In general, all groups exhibited the osteointegration between host bones and titanium implants, which was evidenced by the close contact between basal bone layer and implants. Specifically, these histological results were in accordance with the micro-CT observation, showing that the highest amount of new bones were generated in the GNPs-iPRF group (**Figure 4**a,b). At four weeks post-implantation, new osteoid (blue) was distributed around the new woven bones (red) in all three groups. Compared with the other two groups, more bone matrix and new woven bone were observed in GNPs-iPRF group (Figure 4a). At eight weeks, the newly formed bones gradually matured and remodeled into lamellar bones, which were also stained red. Apparently, more mature lamellar bones could be clearly detected in GNPs-iPRF group (Figure 4b). Further, semiquantitative analysis based on the tissue sections was performed to evaluate the space maintenance of newly formed bone tissues (Figure 4c). In particular, the area of new bone (denoted as NBA), the height of new bone (denoted as NBH), and the angle between the Schneiderian membrane and the implant (denoted as MIA) were assessed. Lowest values regarding NBA, NBH, and MIA were observed in the control group. By contrast, the GNPs-iPRF group showed significantly higher values of NBA, NBH, and MIA than those

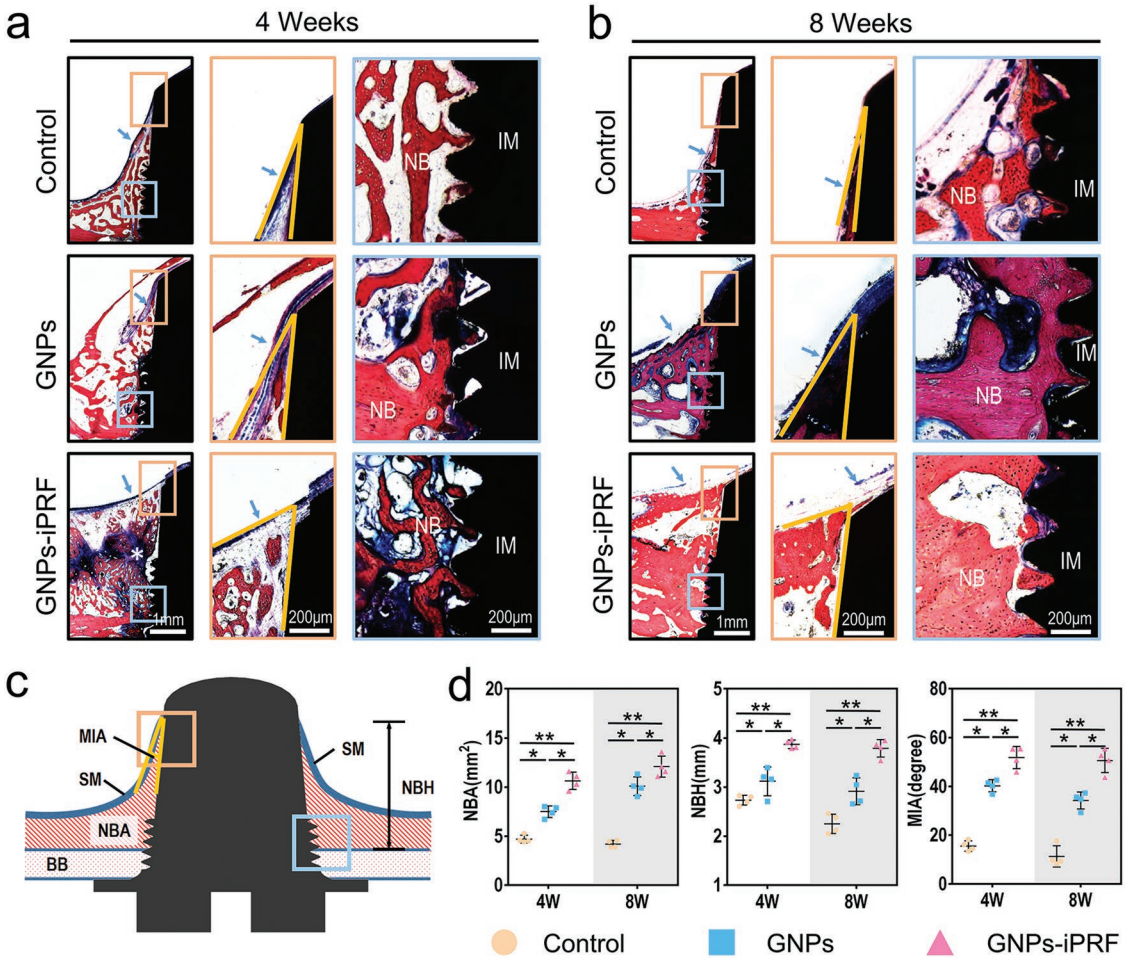

Figure 4. Histological analysis of bone formation in a rabbit sinus augmentation model. a,b) Stevenel's blue and Van Gieson's picrofuchsin staining (VG staining) was performed on hard tissue sections at 4 and 8 weeks post-implantation. The results showed that more new bone was detected in GNPs-iPRF compared to two other groups. In addition, at four weeks, a different histological phenomenon from the other two groups was observed in GNPs-iPRF group: a piece of bone matrix (marked as *) divided the new bone into two parts. As shown in (c), two areas (orange box and azure box) were selected to further observe the new bone formation. Red represents new bone, blue represents bone matrix, and black represents implant. c) Graphics of semiquantitative analysis regarding new bone area (NBA), new bone height (NBH), and the angle between the membrane and the implant (MIA). SM was interpreted as the continuous periosteal-like structure (shown by the blue arrow in (a) and (b)). d) Semiquantitative analysis showed that NBA, NBH, and MIA were greater in GNPs-iPRF group than the other two groups at 4 and 8 weeks post-implantation ($n = 4$). SM: Schneiderian membrane, BB: basal bone, IM: implant, NB: new bone, NBA: new bone area, NBH: new bone height, MIA: the angle between the membrane and the implant, * $P < 0.05$, ** $P < 0.01$.

of GNPs and control groups (Figure 4d). Moreover, comparison between 4 and 8 weeks post-implantation showed that the values of NBH and MIA in control group at eight weeks post-implantation decreased significantly compared to the early time point. Yet in GNPs-iPRF group, no obvious decrease in the values of NBH and MIA could be observed at two different time points (Figure S16, Supporting Information). This suggested that the treatment using GNPs-iPRF gels led to the enhanced bone formation but also less bone resorption over time, while newly formed bones gradually resorbed at a later time point in the control group. It was worth mentioning that lamellar bone could still be observed at the implant apex in GNPs-iPRF group at eight weeks post-implantation, in contrast to the control group where no bone remained between Schneiderian membrane and the implant apex (Figure S17, Supporting Information). Such phenomenon of new bone resorption was reported in previous studies that the resorption of newly formed bones within the sinus cavity was presumably due to the mechanical stimuli generated at the sinus site during respiration.[42] Remarkably, the sinus cavities filled by GNPs-iPRF or GNPs gels showed no obvious bone resorption but maturation of bone tissues was displayed when treated with GNPs-iPRF gels.

Notably, a different pattern of new bone formation was observed at four weeks post-implantation for the defects treated with GNPs-iPRF hydrogels as compared to the other two groups, that is, more woven bones were formed close to both the basal bone and the Schneiderian membrane, leaving the intermediate area filled with more immature bone tissues (Figure 4a, marked with *). These results encouraged us to further investigate the pattern of bone formation at different time points.

2.4. Different Patterns of New Bone Formation in Sinus Cavity

To further explore the evolutionary change of bone formation, we performed sequential fluorescence labeling. Different fluorescent-labeled mineral dyes were injected intramuscularly at 2 (yellow), 4 (green), and 7 (red) weeks, indicating the spatiotemporal information of new bone growth. It was observed that the sequence of new bone formation was creeping along the direction from basal bone to Schneiderian membrane in both control and GNPs groups (**Figure 5**a); this was similar to the previous observations of bone regrowth patterns in sinus defects.[43] Microscopic images of higher magnification revealed that newly formed bones were gradually lifted up from the basal bone to the Schneiderian membrane side (Figure 5b). In contrast, the sequence of bone regeneration in defects treated with GNPs-iPRF hydrogels showed a completely different pattern. It seemed that bone regrowth initiated from both the basal bone and membrane sides, and regrew along both basal-to-membrane and membrane-to-basal directions. Especially, there were more red fluorescent signals representing osteogenesis at a later time point (seven weeks) concentrated at the middle area of the elevated bone tissues (Figure 5a, marked with *), indicating new bones might regrow from both basal and membrane sides to bridge the gap between two osteogenic sources in GNPs-iPRF group. Additionally, the mineral deposition rate and new bone area in GNPs-iPRF group were higher than the other two groups (Figure S18, Supporting Information).

These interesting histological observations suggested that there might be two osteogenic sources within the sinus cavities that can induce bone regeneration, i.e., basal bone and Schneiderian membrane. Such theory has been proposed previously, but the conclusion about the origin of osteogenesis are still under debate.[44] A majority of studies have shown new bone formation stemming from the basal bone in the sinus cavities,[43] while some studies have revealed that the Schneiderian membrane could also function as the periosteum-like structure to offer osteogenic potential and induce new bone formation.[44,45]

To gain further insight into the different osteogenic pattern within sinus cavity, histological and fluorescence labeling analysis (4d injection of calcein, 10d injection of alizarin red) in earlier time points were performed in control group. Intriguingly, new bone regrew from both the basal bone and the membrane sides at early stage of bone regeneration (within two weeks post-implantation), even though no filling biomaterials have been introduced except the metal implant. This was confirmed by both VG staining tissue sections (Figure 5c) and sequential fluorescent labeling (Figure 5c). With a prominent twist, the pattern of osteogenesis gradually transferred from a bidirectional fashion at early stage into a unidirectional fashion characterized by new bone formation mainly contributed from the basal bone in control group (Figure 5d). On the contrary, by filling the sinus cavities with GNPs-iPRF hydrogels, the bone resorption was dramatically reduced as reflected by the bone regrowth in a bidirectional fashion.

2.5. The Effect of GNPs-iPRF Gels on Bone Resorption in Sinus Cavity

We speculated the change in the pattern of osteogenesis to be related to bone resorption caused by the continuous stimuli from the air pressure in the maxillary sinus, which has been often observed in clinic (**Figure 6**a). Asai et al. verified that the resorption of endosinus bone was counteracted by eliminating air pressure in the sinus through occluding the rabbit's nasal cavity.[42] In order to quantify the air pressure on the Schneiderian membrane and analyze its influence on new bone formation in elevated Schneiderian membrane area, we established a simplified finite element model of sinus augmentation to calculate the value of pressure intensity (Figure S19, Supporting Information). To this end, the material properties of blood clots (Young's modulus = 6.7 kPa), GNPs colloidal gels (Young's modulus = 9.2 kPa), and GNPs-iPRF DN gels (Young's modulus = 32.9 kPa) were sequentially assigned to the spatial domain (Figure 6b and Figure S20, Supporting Information). The pressure caused by respiration was statically loaded on the Schneiderian membrane to simulate the stress condition of the elevated area and analyze the strain distribution. After the finite element calculation, the strain maps of the above three groups were obtained. According to Wolff's law, all bone filling materials are influenced by the external strain, to which bone tissues will respond.[46] The unit from bone tissues that responds to mechanical environment and generates a physiological response is defined as "bone healing unit." The microstrain from 50 to 3000 $\mu\varepsilon$ of bone healing unit is beneficial for bone

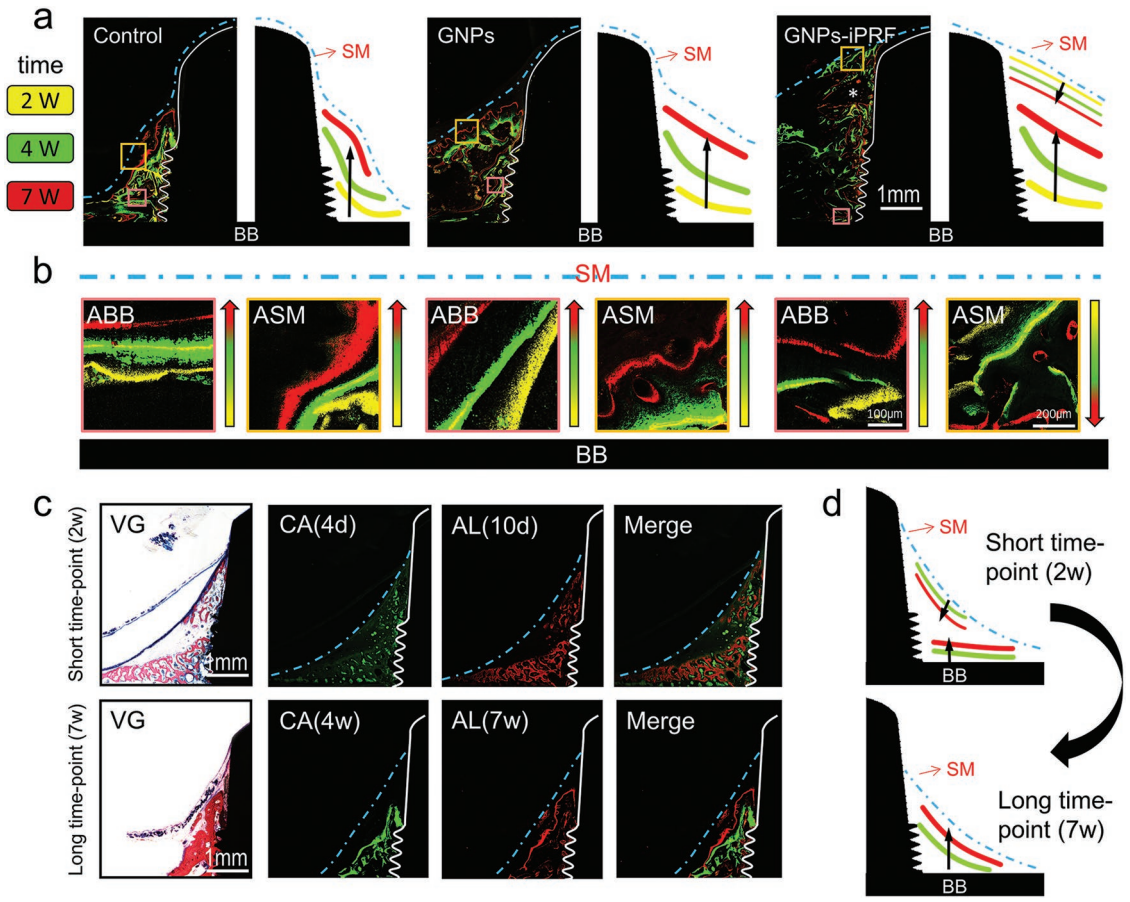

Figure 5. Evolutionary changes of bone formation in a rabbit sinus augmentation model. a) Tetracycline (yellow) was injected at two weeks, calcein (green) at four weeks, and alizarin red (red) at seven weeks for sequential fluorescent labeling. Yellow (2w)–green (4w)–red (7w) fluorescently labeled mineral deposition was observed from basal bone to implant apex in control and GNPs groups. In GNPs-iPRF group, the red area was diffusely distributed, which divided the new bone area at the elevated site into two parts (marked as *). b) Two regions of interest (ROI) were selected: 1) area near basal bone (ABB (b), pink box); 2) area underneath the SM near the implant apex (ASM (b), orange box). The results showed that control and GNPs groups exhibited similar trends in the two ROIs: yellow-green-red area deposition could be observed from basal bone to the implant apex. In GNPs-iPRF group, the ABB area showed similar trends to the other two groups. Regarding ASM, the mineral deposition sequence was in stark contrast to the other two groups, which could be described as yellow-green-red area from implant apex pointed to the basal bone. c) A histological analysis and sequential fluorescent labeling (4d injected with calcein, 10d injected with alizarin red) were performed on the control group at an earlier time point compared with long-term time point. Unlike long-term results, VG staining showed that the new bone was observed underneath the Schneiderian membrane and above the basal bone, among which were connected by immature bone matrix. The results of sequential fluorescent labeling showed new bone formation from basal bone upwards to Schneiderian membrane downwards was detected in control group at two weeks. d) The schematic diagram for the alteration of osteogenic pattern at different time points. SM: Schneiderian membrane, BB: basal bone, VG: VG staining, CA: calcein, AL: alizarin red.

healing process.[46,47] The strain maps showed that the apex and its periphery of the implant in control group were red (greater than 3000 με), and the number of bone healing unit for osteogenesis mechanics accounted for 71.2% of the total element (Figure 6c). Therefore, the blood clots around the implant apex (stress concentration area) were not able to effectively resist the pressure formed in the maxillary sinus during respiration, so that the de novo bone in the sinus failed to maintain its contour in control group at 4 and 8 weeks post-implantation, eventually leading to its collapse (Figure 4a,b and Figure S17, Supporting Information). At the same time, it was calculated that there was no high-concentration area (red area) between the Schneiderian membrane and the implant apex in the GNPs-iPRF group, where the value of bone healing unit accounted for 98.13% of the total element. Correspondingly, the formation of lamellar bone between the membrane and the implant apex was observed in histological staining at eight weeks (Figure S17, Supporting Information). The above results suggested that the difference in grafting materials resulted in a relative change in stress and strain at the apex and periphery of the implant, which in turn affected new bone formation and remodeling in the elevated Schneiderian membrane area.

It is extensively accepted that the mechanical microenvironment and stimulation are closely related to bone formation and bone remodeling.[1,6] To demonstrate that bone resorption in sinus cavities is related to mechanical stimuli, we performed immunofluorescence staining on Periostin (POSTN), which is a biomechanically responsive protein related to bone regeneration and remodeling.[48] Specifically, under the effect of pulling and pushing, cells could sense the ambient mechanical

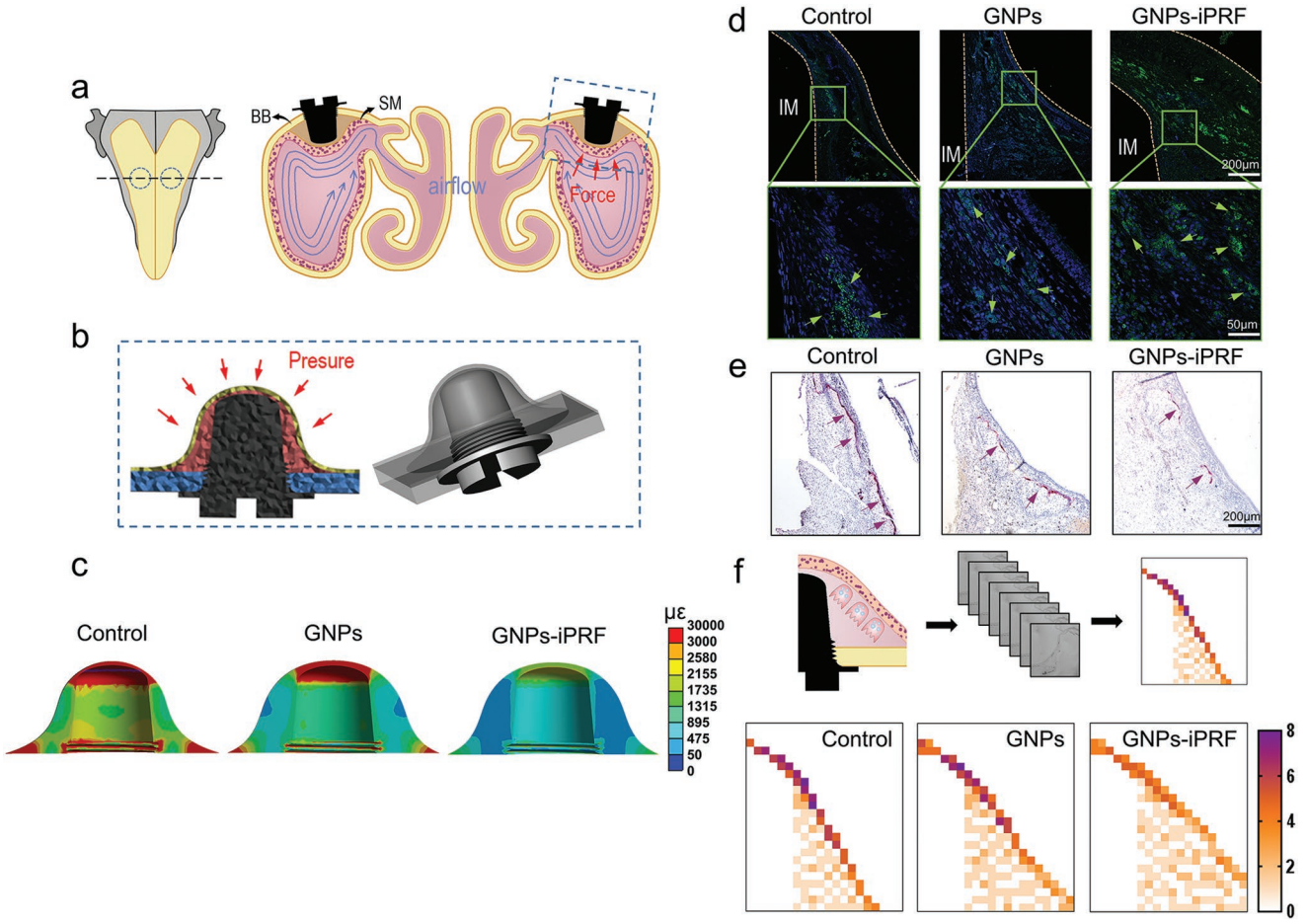

Figure 6. The effect of GNPs-iPRF hydrogels on bone resorption in sinus cavity. a) The compressive stress caused by the displacement of the Schneiderian membrane throughout the bone formation and reconstruction process after sinus augmentation. b) The sinus augmentation model was simplified and established (Figure 7a blue dotted box), and the Schneiderian membrane was statically loaded with pressure caused by normal respiration to simulate the stress condition in each group of elevated areas and analyze the strain distribution. c) Strain maps of control, GNPs, and GNPs-iPRF groups. d) POSTN immunofluorescence staining was performed on sinus specimens at two weeks post-implantation, which represented the central of bone biomechanical response. The staining results reflected that POSTN was found in the three groups at wedge-shaped area between Schneiderian membrane and the implant. POSTN in GNPs-iPRF was expressed more than the other two groups. The green arrow was pointed to the POSTN positively expressed area. e) TRAP staining (the expression of this staining represented the function of osteoclasts) was performed on maxillary sinus specimens of each group at two weeks post-implantation, and the results showed that a large amount of TRAP activity was observed at the implant apex and under Schneiderian membrane (high strain area) in control group, while the TRAP activity was minimal in GNPs-iPRF group. The purple arrow was pointed to the TRAP-positive expression area. f) The tissue sections stained with TRAP were divided into a mesh with 24 × 50 units, and the unit with TRAP-positive expression was marked as 1, while those without TRAP-positive expression were marked as 0. The addition of the corresponding number was conducted on ten consecutive specimens from three groups and heat maps were drawn subsequently. The results suggested that the high expression area of TRAP was basically consistent with the high strain area in the finite element analysis. SM: Schneiderian membrane, BB: basal bone, IM: implant.

microenvironment, and correspondingly, produce biochemical activity within suitable mechanical stimuli, that is, demonstrating highly expressed POSTN.[48,49] According to previous studies, positive POSTN expression is strongly correlated with tissue repair and wound healing promotion, revealing a function in angiogenesis and osteogenesis beyond its role as a structural protein.[50] Strikingly, we detected positive POSTN expression at early stage (two weeks post-implantation) in all groups at the wedge-shaped area where newly formed bones located (Figures 6d and 5a,c). This indicated the locations of stress concentration and was coincident to the result of our simulation. Specifically, significantly higher positive POSTN expression was observed in the defect treated by GNPs-iPRF gels as compared to those of control and GNPs groups (Figure 6d and Figure S21a, Supporting Information).

Previous studies also have shown the relationship between POSTN expression and osteoclast activities, i.e., the downregulation of POSTN expression leads to a substantial increase in the activity of osteoclasts in bone tissues and following bone resorption.[49,51] Therefore, we further evaluated the function of osteoclasts in the tissue sections by tartrate-resistant acid phosphatase (TRAP) staining, in which osteoclasts were stained purple. We noticed that in the control group significantly higher TRAP activity was particularly located at the regions under the Schneiderian membrane. In contrast, minimal TRAP

activity was observed in the defects treated with GNPs-iPRF gels, indicating lower osteoclasts activity (Figure 6e and Figure S21b, Supporting Information). We further analyzed the intensity and location of TRAP expression by summarizing a series of consecutive tissue sections for each group and drawing into a heat map as shown in Figure 6f. The result confirmed that the regions of higher TRAP expression in the control group overlapped with the regions of stress concentration based on our simulated strain maps (Figure 6c). Collectively, these results provided solid evidences to prove that the bone formation and resorption in the sinus augmentation model is strongly related to the mechanical stimuli. Apparently, bones under Schneiderian membrane were directly exposed to the high compressive stress generated from the respiration, which led to higher osteoclastic activity and subsequent bone resorption. However, the presence of GNPs-iPRF or GNPs hydrogels obviously alleviated, if not inhibited, bone resorption stemming from the unfavorable stress concentration, thereby achieving enhanced bone regeneration within sinus cavities. This might result from the favorable mechanical properties of GNPs-iPRF DN gels which could provide local adaptability to the irregular-shaped cavity and maintain the bulk stability by dissipating the external stress from the rhythmic respiration.

2.6. The Effect of GNPs-iPRF Gels on Angiogenesis

In addition to biomechanical signals, the presence of biochemical signals also plays a dominant role in inducing bone regeneration.[2,3] Previous studies have demonstrated the capacity of injectable GNPs colloidal gels for sustained delivery of biomolecules such as BMPs, fibroblast growth factors (FGFs), due to the inherent porous matrix of gelatin, large specific surface area, strong affinity to proteins by electrostatic and hydrophobic interactions, and tunable degradation rates.[8,37,41] Here in this study, we suggested the GNPs within the DN gels as delivery vehicles for sustained release of bioactive components from iPRF, thereby providing bioactivity to induce cell regrowth and tissue regeneration. According to enzyme-linked immunosorbent assay (ELISA) examination, GNPs-iPRF showed the capacity of more than three weeks sustained release of multiple growth factors from the iPRF, including VEGF, platelet derived growth factor-BB (PDGF-BB), TGF-β, and insulin-like growth factor-1 (IGF-1) (**Figure 7**a). In comparison, the study in vitro of growth factors released from pure iPRF gels showed significantly higher burst release at the initial time points than the DN gels, and all the growth factors leaked out after two weeks in vitro incubation, which is similar to previous studies stated[16,52] (Figure 7a). Compared to the previous studies, GNPs-iPRF displayed satisfied effect as a delivery vehicle regarding controlled release of factors. For instance, Barati et al. incorporated BMP-2, VEGF, and other growth factors into a nanogel based on polyethylene glycol for large bone defects and found out the gel could maintain its sustained release on the 21th d.[53] Similarly, Zhao et al. fabricated an injectable hydrogel to deliver VEGF and PDGF-BB for angiogenesis and detected slow release of both growth factors on the 15th d.[20] Compared with the above materials, GNPs-iPRF gel, by loading concentrated autologous blood growth factor, was cheaper, simpler to fabricate, and easier to be accepted by patients. While compared with pure autologous platelet- and plasma-derived protein fibrin scaffold, GNPs-iPRF gel prolonged the release period and bypassed the burst release of the factors.

In particular, VEGF, PDGF-BB, and IGF-1 from iPRF are well-known angiogenic growth factors which are prerequisite for later osteogenesis.[54] Therefore, we speculated that the prolonged release of these growth factors owing to the presence of GNPs might provide continuous inductive signals at the defect sites via establishing local neovascularization network at the early stage.

In order to verify the angiogenesis potential of GNPs-iPRF hydrogels, the conditioned mediums were cultured with human umbilical vein endothelial cells (HUVECs) in vitro and we evaluated the vasculature qualitatively and quantitatively correspondingly. The results of tube formation showed that the number of tubes, the number of tube nodes, and the total tube lengths of the vascular network formed by HUVECs in GNPs-iPRF conditioned medium were significantly higher than cells cultured in GNPs conditioned medium or tissue culture plates; this displayed that the control group was consisted of only medium while there were plentiful growth factors released from GNPs-iPRF gels in the medium to promote the angiogenesis (Figure 7b,c). Further qPCR results revealed that the mRNA levels of *VEGF*, *Col-1*, and *Ang-1* were significantly higher for HUVECs cultured in GNPs-iPRF conditioned medium than those of the GNPs and control groups (Figure 7d).

Subsequently, the angiogenic abilities among GNPs-iPRF, GNPs, and iPRF gels were compared in the back of nude mice. Moreover, more angiogenesis was observed in GNPs-iPRF and iPRF groups after two weeks implantation (Figure 7e). Nevertheless, the presence of iPRF gel could not be observed in iPRF group, suggesting its degradation rate was faster than that of bone tissue regeneration. Further H&E staining of the sinus tissue sections confirmed pronounced angiogenesis in GNPs-iPRF group as compared with GNPs and control groups at four weeks (Figure 7f). The histomorphometric statistics of the neovascularization demonstrated that GNPs-iPRF was superior compared to the other two groups in terms of the number, density, and diameter of newly formed blood vessels (Figure 7g). These results suggested that the GNPs-iPRF gels were biologically active and could accelerate early vascularization, ultimately leading to the desirable osteogenic effects. In addition, the effects of GNPs-iPRF on cellular immunity, migration, and the mechanical strength of materials on cell differentiation have not been explored in this study. Among previous studies, it was shown that in addition to promoting angiogenesis, various growth factors within iPRF could also promote cell proliferation, cell migration, and regulate the macrophages to transform to the anti-inflammation state.[15,55] It was also proven that mechanical features such as stiffness, stress relaxation, and creep can significantly steer stem cell fate.[4,22] Future study regarding GNPs-iPRF should be emphasized on cellular and molecular levels to further investigate what other factors could have contributed to the favorable osteogenic effect.

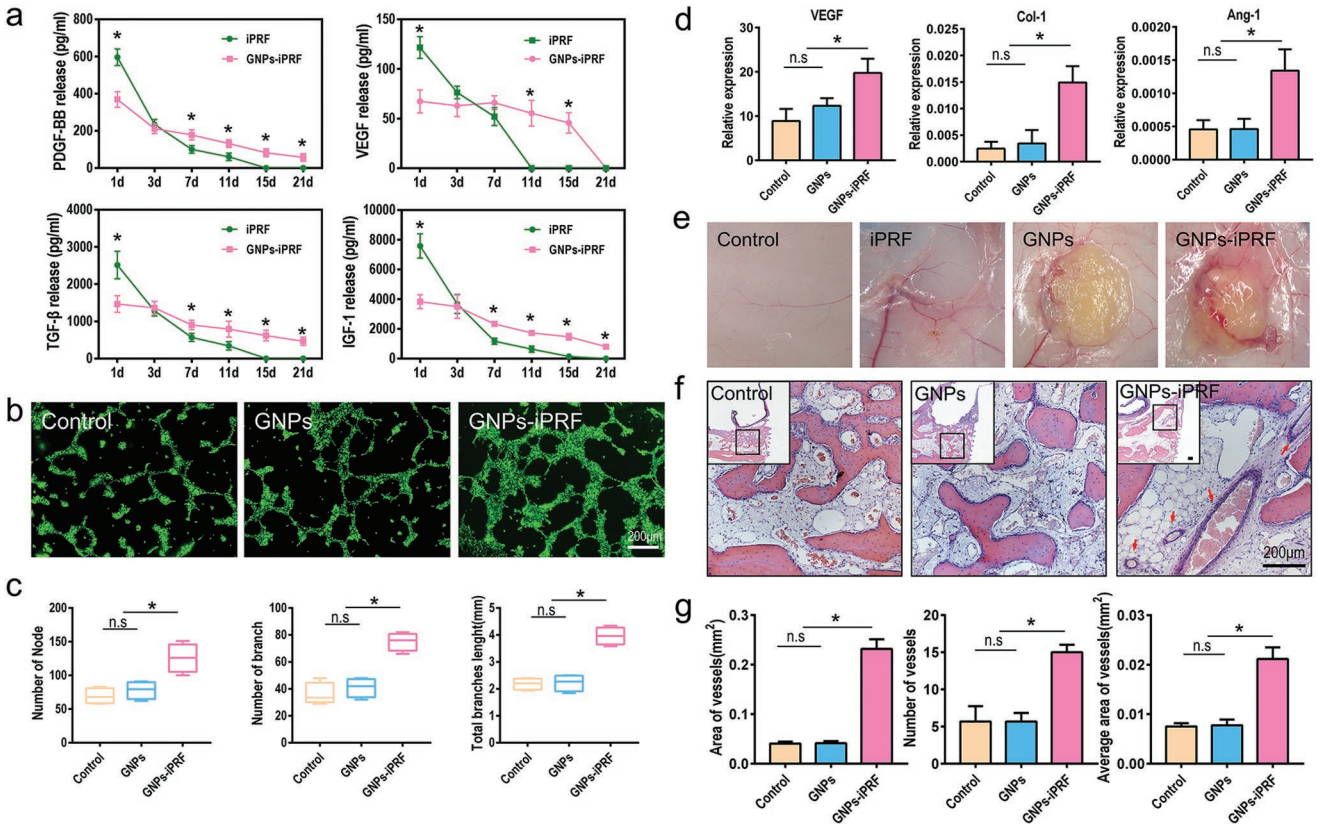

Figure 7. The effect of GNPs-iPRF hydrogels on angiogenesis. a) ELISA was used to detect the release of the four major growth factors contained in iPRF and GNPs-iPRF ($n = 3$). The results showed that GNPs-iPRF possessed a better sustained release effect than iPRF. On day 1, a significantly burst release was observed in iPRF, and the releasing quantity of GNPs-iPRF was about half that of iPRF. In addition, multiple growth factors in iPRF were not detectable on day 15, while GNPs-iPRF could still be detected on day 21. b) Conditioned medium of each group was cocultured with HUVECs and vascular tube formation assay was performed. c) Semiquantitative analysis of vascular tube formation ($n = 3$). The result showed that the number of tubes, the number of tube nodes, and the total tube lengths in the GNPs-iPRF group were all greater than those in the other two groups. d) Conditioned medium of each group were cocultured with HUVECs and qRT-PCR was conducted correspondingly ($n = 3$). The results showed that the mRNA levels of *VEGF*, *Col1*, and *Ang-1* were significantly higher in GNPs-iPRF group than those in GNPs and control groups. e) After the same volumes of GNPs-iPRF, GNPs, and iPRF gels were placed in the back of the nude mice for 14 d, more blood vessels were observed obviously in GNPs-iPRF and iPRF groups, and the presence of GNPs and GNPs-iPRF could still be detected 14 d later, but not iPRF gel. f) H&E staining was performed on the tissue sections of sinus augmentation models at four weeks post-implantation, the results showed that obvious blood vessel formation and even larger blood vessels were observed in GNPs-iPRF group. g) The histomorphometric statistics of the above-mentioned neovascularization demonstrated that GNPs-iPRF was superior to other two groups regarding the number, density, diameter of new blood vessels ($n = 4$). * $P < 0.05$.

3. Conclusion

In summary, we developed biphasic hydrogels based on gelatin nanoparticles and iPRF, which has shown injectability and self-healability, as well as significantly enhanced toughness values and degree of deformation than each component can achieve separately. Such remarkable mechanical properties were demonstrated to be attributed to the double network structure of the hydrogels, in which iPRF offered a primary covalent network to maintain structural stability, while the colloidal network of GNPs provided sacrificial bonds to dissipate energy upon loading. More importantly, the DN hydrogel offered local adaptability to the topographical and mechanical conditions of the irregular-shaped bone defects. Remarkably, the treatment of DN gels can reverse the long-existing problematic issue of bone resorption in sinus augmentation surgery, presumably related to the adaptable hydrogels that can dissipate the destructive compression generated by respiration in the sinus cavity. We suggested that the adaptable and bioactive DN hydrogels can achieve enhanced tissue regeneration while maintaining long-term bone mass by accommodating the irregular shape of the defects, providing physiologically relevant environment and withstanding the external loadings from regular physiological activities, thus offering a valuable solution for the clinical challenges in treating bone defects of high degree of local complexity.

4. Experimental Section

Materials Synthesis: Gelatin nanoparticles were prepared by a two-step desolvation method. 7 mL of whole blood without anticoagulant was centrifuged at 700 rpm for 3 min by a duo-Centrifuge (Process for iPRF, Nice, France). Subsequently, 1 mL yellowish liquid-like iPRF was collected from the upper layer of the blood.

Cell Behavior Assessment: For angiogenic differentiation, HUVECs were seeded in a mixture containing DMEM, 1% penicillin–streptomycin,

and 20% FBS. All the cells were then cultured at 37 °C in a humidified atmosphere which was kept at 5% CO_2.

Two groups of sterile materials (GNPs, GNPs-iPRF) were both incubated in DMEM medium containing 20% FBS and the supernatant of 1 d was selected to prepare 20% conditioned medium. The conditioned mediums were cultured with HUVECs in vitro and evaluated vasculature qualitatively and quantitatively by tube formation assay and PCR.

Statistical Analysis: All the results are calculated as mean ± sd. Statistical analyses were conducted using ANOVA by SPSS Statistics version 20.0 (IBM Corp., Armonk, NY) and Graphpad Prism Version 7 (Graphpad Software, USA). Differences were considered statistically significant at the $p < 0.05$.

Please see the Supporting Information for details. All animal experiments were performed according to protocols approved by the Chongqing Medical University Ethics Review Committee (CQHS-IRB-2018-07).

Supporting Information

Supporting Information is available from the Wiley Online Library or from the author.

Acknowledgements

Z.M. and K.C. contributed equally to this work. The authors would like to thank Dr. Li Chen from Analytical & Testing Center Sichuan University for her help with micro-CT scanning and analysis. The authors would like to thank Annie Shrestha from University of Toronto for her help with the language editing and revision. This work was supported by the National Key Research and Development Program of China (No. 2018YFA0703000), the National Natural Science Foundation of China (Nos. 31870957, 81701031, and 31871464), the Fundamental Research Funds for the Central Universities of China (No. DUT15RC (3)113), Postdoctoral Science Foundation of China (No. 2017M622981), the Chongqing Special Postdoctoral Science Foundation (No. XmT2018009), and Chongqing Research Program of Basic Research and Frontier Technology (No. cstc2018jcyjAX0200).

Conflict of Interest

The authors declare no conflict of interest.

Keywords

adaptable hydrogels, biomechanical stimuli, bone regeneration, double-network hydrogels, iPRF

Received: October 16, 2019
Revised: December 19, 2019
Published online:

[1] D. Lopes, C. Martins-Cruz, J. F. Mano, *Biomaterials* **2018**, *185*, 240.
[2] K. D. Hankenson, K. Gagne, M. Shaughnessy, *Adv. Drug Delivery Rev.* **2015**, *94*, 3.
[3] E. A. Bayer, R. Gottardi, S. R. Little, *J. Controlled Release* **2015**, *219*, 129.
[4] J. H. Wen, L. G. Vincent, A. J. Engler, *Nat. Mater.* **2014**, *13*, 979.
[5] B. Trappmann, J. E. Gautrot, W. T. Huck, *Nat. Mater.* **2012**, *11*, 642.
[6] C. Liu, R. Carrera, A. B. Castillo, *Bone* **2018**, *108*, 145.
[7] S. Pina, J. M. Oliveira, R. L. Reis, *Adv. Mater.* **2015**, *27*, 1143.
[8] H. Wang, Q. Zou, S. C. Leeuwenburgh, *J. Controlled Release* **2013**, *166*, 172.
[9] W. Zhang, X. Wang, X. Jiang, *Biomaterials* **2011**, *32*, 9415.
[10] J. Tan, M. Zhang, G. Liang, *ACS Nano* **2019**, *13*, 5616.
[11] Z. A. Cheng, A. Alba-Perez, M. Salmeron-Sanchez, *Adv. Sci.* **2019**, *6*, 1800361.
[12] J. Y. Hong, M. S. Kim, U. W. Jung, *Clin. Oral Implants Res.* **2016**, *27*, e199.
[13] E. Anitua, P. Nurden, S. Padilla, *Biomaterials* **2019**, *192*, 440.
[14] R. Shah, T. M. Gowda, D. S. Mehta, *J. Prosthet. Dent.* **2019**, *121*, 391.
[15] X. Wang, Y. Zhang, R. J. Miron, *Platelets* **2018**, *29*, 48.
[16] R. J. Miron, M. Fujioka-Kobayashi, J. Choukroun, *Clin. Oral Invest.* **2017**, *21*, 2619.
[17] a) X. Liu, Y. Yang, L. Zhu, *Acta Biomater.* **2017**, *62*, 179; b) A. Noori, S. J. Ashrafi, T. J. Webster, *Int. J. Nanomed.* **2017**, *12*, 4937.
[18] M. Liu, X. Zeng, N. He, *Bone Res.* **2017**, *5*, 17014.
[19] K. Flegeau, R. Pace, P. Weiss, *Adv. Colloid Interface Sci.* **2017**, *247*, 589.
[20] N. Zhao, A. Suzuki, Y. Wang, *ACS Appl. Mater. Interfaces* **2019**, *11*, 18123.
[21] J. Xu, Q. Feng, L. Bian, *Biomaterials* **2019**, *210*, 51.
[22] A. S. Mao, J. W. Shin, D. J. Mooney, *Biomaterials* **2016**, *98*, 184.
[23] A. J. Engler, S. Sen, D. E. Discher, *Cell* **2006**, *126*, 677.
[24] O. Chaudhuri, L. Gu, D. J. Mooney, *Nat. Mater.* **2016**, *15*, 326.
[25] G. R. Fercana, S. Yerneni, J. A. Phillippi, *Biomaterials* **2017**, *123*, 142.
[26] C. Ma, Y. Shi, G. Yu, *Angew. Chem., Int. Ed.* **2015**, *54*, 7376.
[27] J. K. Sahoo, M. A. VandenBerg, M. J. Webber, *Adv. Drug Delivery Rev.* **2018**, *127*, 185.
[28] a) K. Zhang, Z. Jia, L. Bian, *Adv. Sci.* **2018**, *5*, 1800875; b) R. Song, J. Zheng, Y. Wang, *Int. J. Biol. Macromol.* **2019**, *134*, 91.
[29] H. Wang, M. Bongio, S. C. Leeuwenburgh, *Acta Biomater.* **2014**, *10*, 508.
[30] H. Wang, M. B. Hansen, S. C. Leeuwenburgh, *Adv. Mater.* **2011**, *23*, H119.
[31] M. Diba, H. Wang, S. C. Leeuwenburgh, *Adv. Mater.* **2017**, *29*, 1604672.
[32] J. P. Gong, Y. Katsuyama, Y. Osada, *Adv. Mater.* **2003**, *15*, 1155.
[33] B. B. Mendes, M. Gomez-Florit, M. E. Gomes, *Adv. Drug Delivery Rev.* **2018**, *129*, 376.
[34] Y. Mao, M. Cates, H. Lekkerkerker, *Phys. A: Stat. Mech. Appl.* **1995**, *222*, 10.
[35] a) A. Dinsmore, D. Weitz, *J. Phys.: Condens. Matter* **2002**, *14*, 7581; b) A. Dinsmore, V. Prasad, D. Weitz, *Phys. Rev. Lett.* **2006**, *96*, 185502.
[36] R. G. Larson, Vol. *86*, *The Structure and Rheology of Complex Fluids (Topics in Chemical Engineering)*, Oxford University Press, New York **1999**, p. 108.
[37] H. Wang, O. C. Boerman, S. C. Leeuwenburgh, *Biomaterials* **2012**, *33*, 8695.
[38] Q. Wang, L. Wang, C. Berkland, *Adv. Mater.* **2008**, *20*, 236.
[39] a) B. B. Mendes, M. Gomez-Florit, M. E. Gomes, *Nanoscale* **2018**, *10*, 17388; b) A. K. Gaharwar, N. A. Peppas, A. Khademhosseini, *Biotechnol. Bioeng.* **2014**, *111*, 441.
[40] Z. Lu, S. Liu, L. Zheng, *Biomaterials* **2019**, *218*, 119190.
[41] J. van der Stok, H. Wang, H. Weinans, *Tissue Eng., Part A* **2013**, *19*, 2605.
[42] S. Asai, Y. Shimizu, K. Ooya, *Clin. Oral Implants Res.* **2002**, *13*, 405.
[43] a) A. Scala, D. Botticelli, N. P. Lang, *Clin. Oral Implants Res.* **2012**, *23*, 175; b) E. De Santis, N. P. Lang, D. Botticelli, *Clin. Oral Implants Res.* **2017**, *28*, 503.
[44] Q. Rong, X. Li, D. Y. Huang, *Br. J. Oral Maxillofac. Surg.* **2015**, *53*, 607.

[45] A. Graziano, L. Benedetti, M. Aimetti, *J. Cell. Physiol.* **2012**, *227*, 3278.
[46] D. S. Elliott, K. J. Newman, C. G. Moran, *Bone Jt. J.* **2016**, *98-B*, 884.
[47] H. M. Frost, *Angle Orthod.* **2004**, *74*, 3.
[48] N. Bonnet, K. N. Standley, S. L. Ferrari, *J. Biol. Chem.* **2009**, *284*, 35939.
[49] J. Du, M. Li, *Cell. Mol. Life Sci.* **2017**, *74*, 4279.
[50] a) N. Bonnet, S. J. Conway, S. L. Ferrari, *Proc. Natl. Acad. Sci. USA* **2012**, *109*, 15048; b) N. Bonnet, P. Garnero, S. Ferrari, *Mol. Cell. Endocrinol.* **2016**, *432*, 75.
[51] H. Rios, S. V. Koushik, S. J. Conway, *Mol. Cell. Biol.* **2005**, *25*, 11131.
[52] S. Wend, A. Kubesch, S. Ghanaati, *J. Mater. Sci.: Mater. Med.* **2017**, *28*, 188.
[53] D. Barati, S. R. P. Shariati, E. Jabbari, *J. Controlled Release* **2016**, *223*, 126.
[54] a) J. Huang, H. Yin, H. Xie, *Theranostics* **2018**, *8*, 2435; b) K. Hu, B. R. Olsen, *J. Clin. Invest.* **2016**, *126*, 509.
[55] a) J. Zhang, C. Yin, Y. Zhang, *J. Biomed. Mater. Res., Part A* **2020**, *108*, 61; b) J. Leotot, L. Coquelin, N. Chevallier, *Acta Biomater.* **2013**, *9*, 6630.

